



Journal of Applied and Computational Mechanics



Research Paper

Simulation of Hydraulic Fracture Propagation in Fractured Coal Seams with Continuum-discontinuum Elements

Haifeng Zhou^{1,2}, Hui Gao³, Chun Feng⁴, Zizheng Sun^{5,6}

¹ College of Energy Engineering, Xian University of Science and Technology, Yata Road 58, Xian, 710054, China, Email: 282090097@qq.com

² Shenhua Shendong Coal Group Corporation Ltd, Daliuta Town Shenmu County, Yulin, 719315, China

³ School of Civil and Transportation Engineering, Hebei University of Technology, Xiping Road 5340, Tianjin, 300401, China, Email: 2370706591@qq.com

⁴ Institute of Mechanics, Chinese Academy of Sciences, 15 Beishihuan Xi Lu, Haidian District, Beijing, 100190, China, Email: fengchun@imech.ac.cn

⁵ School of Qilu Transportation, Shandong University, Jingshi Road 17923, Jinan, 250061, China, Email: zizheng.sun@sdu.edu.cn

⁶ Shenzhen Research Institute of Shandong University, No. 19, Gaoxin South 4th Road Nanshan District, Shenzhen Guangdong, China

Received May 19 2021; Revised September 29 2021; Accepted for publication October 04 2021.

Corresponding author: Zizheng Sun (zizheng.sun@sdu.edu.cn)

© 2021 Published by Shahid Chamran University of Ahvaz

Abstract. Creating new fracture networks in coal seams with natural fractures through hydraulic fracturing techniques is an effective method for exploiting coal-bed methane. In this paper, a continuum-discontinuum element method (CDEM) is developed for simulating and assessing hydraulic fracture propagation in coal seams. An elastic-damage-fracture model is proposed for capturing the deformation and cracking processes of fractured coal. A stress-fracture percolation relation is implemented to simulate the hydro-mechanical coupling processes. The influence of X-direction angles, mechanical strengths, distances and lengths of natural fractures are analyzed in detail. The results are potentially useful to optimize the fracturing design.

Keywords: Continuum-discontinuum element method (CDEM); Hydraulic fracturing; Fractured coal; Hydro-mechanical coupling.

1. Introduction

With the growth of global energy consumption, the exploitation of coal-bed gas has become a hot topic, as the process can be made cleaner and safer by utilizing modern techniques such as hydraulic fracturing. Hydraulic fracturing is a process in which fracturing fluids such as water and supercritical carbon dioxide are injected into coal seams through high pressure or at a high rate to create new fractures and ultimately build a fracture network, which greatly promotes the exploitation of gas. The new fractures, together with natural fractures in coal seams, facilitate the flow of fluid and gas. However, the strong interaction between hydraulic fractures and natural fractures complicates the hydraulic fracturing process. Numerical simulation of hydraulic fracture propagation can guide designers to optimize drilling and fracturing plans.

For modelling the coupled hydro-mechanical continuous-discontinuous process, many methods have been developed, such as i) methods with remeshing strategies [1–6], ii) phase field methods [7–11], iii) mixed mode formulations [12–18], iv) nodal enriched methods (the extended finite element method (XFEM), numerical manifold method (NMM), and phantom node method) [19–25], v) a strong discontinuity embedded approach with the cracking element method (CEM) [26–32], and vi) particle-based methods such as the cracking particle method (CPM) [33–39]. However, the above methods cannot readily and fully consider the permeation of fractures compared with a crack opening model.

In this paper, an explicitly integrated hybrid finite-discrete element method, called the continuum-discontinuum element method (CDEM), is adopted to simulate hydraulic fracturing. The associated coal mass is simulated using block elements, and the discrete crack is modelled using interface elements. An elastic-damage-fracture constitutive relation is utilized to simulate fracture initiation and propagation. A stress and fracture percolation coupling relation is introduced to capture the hydro-mechanical effects. Moreover, the influence of inclinations, distances and lengths of natural fractures and geostress on the interaction of hydraulic fractures and natural fractures is analyzed. The results show that when the natural fractures are located symmetrically on both sides of the injection point, a favorable fracture network is created.

The paper is organized as follows: In Section 1, the principle of the CDEM, the elastic-damage-fracture constitutive equation and the stress-fracture seepage coupling correlation models are introduced. The numerical model is built in Section 2. In Section 3, the simulation results are presented and discussed. Finally, concluding remarks are given in Section 4.





Fig. 1. The numerical model in the CDEM

2. Numerical Methods

2.1 Continuum-discontinuum element method

The CDEM is a hybrid finite-discrete element method that was developed in the generalized Lagrangian system. The CDEM is solved using explicit integration and a global dynamic relaxation algorithm. The theoretical basis of CDEM is Lagrange equation, which is:

$$\frac{d}{dt} \left(\frac{\partial L}{\partial v_i} \right) + \frac{\partial L}{\partial u_i} = Q_i \quad (1)$$

where v_i and u_i is the generalized coordinates, L is the kinetic energy of the system expressed in terms of each generalized velocity and each generalized coordinate, and Q_i is the generalized force.

The numerical model built in the CDEM is composed of blocks and interfaces (see Figure 1). The blocks are discretized with one or more finite elements, and the interfaces are inserted into the block elements. The dashed lines in Figure 1 represent the real interfaces, which are the natural discontinuities in the model, such as joints and faults in the rock. The solid lines, on the other hand, represent the virtual interfaces that are active during crack initiation and propagation or stay closed for transmitting mechanical information.

2.2 Constitutive relation

An elastic-damage-fracture constitutive relation is used for simulating hydraulic fracturing. The blocks comprise four basic parameters, namely, the density, Young's modulus, Poisson's ratio, and internal friction angle. The interfaces include five basic parameters, namely, the normal and shear stiffnesses, strength, normal and shear fracture energies, and internal friction angle.

The linear elastic constitutive relation for the elements is written in incremental form as

$$\begin{cases} \Delta \sigma_{ij} = 2G \Delta \varepsilon_{ij} + \left(K - \frac{2G}{3} \right) \Delta \theta \delta_{ij} \\ \sigma_{ij}(t_i) = \Delta \sigma_{ij} + \sigma_{ij}(t_{i-1}) \end{cases} \quad (2)$$

where $\Delta \varepsilon_{ij}$ and $\Delta \theta$ are the increment strain tensor and the volumetric strain, respectively, K and G are the bulk and shear modulus, respectively, $\Delta \sigma_{ij}$ is the incremental stress tensor, δ_{ij} is the Kronecker mark, t_i and t_{i-1} represent the last and present time steps, respectively.

For the interfaces, the respective normal and shear contact forces F_n and F_s are calculated as:

$$\begin{cases} F_n(t_i) = F_n(t_{i-1}) - k_n A_c [\Delta u_n(t_i) - \Delta u_n(t_{i-1})] \\ F_s(t_i) = F_s(t_{i-1}) - k_s A_c [\Delta u_s(t_i) - \Delta u_s(t_{i-1})] \end{cases} \quad (3)$$

where $\Delta u_n(t_i)$ and $\Delta u_s(t_i)$ are the normal and shear relative displacement (crack opening) at the present time step, respectively, k_n and k_s are the stiffnesses of the interfaces, respectively, and A_c is the interface area.

The linear softening effect is assumed for tensile failure of interfaces as

$$\begin{aligned} & \text{If } F_n(t_i) \geq \sigma_t(t_{i-1}) A_c \\ & \text{Then } F_n(t_i) = \sigma_t(t_{i-1}) A_c \\ & \text{with } \sigma_t(t_{i-1}) = \max \left[f_t - f_t^2 \frac{\Delta u_n(t_{i-1})}{2G_{ft}}, 0 \right] \end{aligned} \quad (4)$$

where f_t is the initial tensile strength, $\sigma_t(t_{i-1})$ is the residual tensile strength at the last time step, and G_{ft} is the tensile fracture energy.



Table 1. Material parameters

Coal mass		
Density ρ	(kg m ⁻³)	2500
Modulus of Elasticity E	(GPa)	5.0
Poisson's ratio ν	(-)	0.28
Virtual interfaces		
c_0	(MPa)	3.0
f_t	(MPa)	3.0
G_{ft}	(Pa m)	0.01
G_{fs}	(Pa m)	0.01
ϕ	(°)	35
k_n, k_s	(MPa/m)	$1 \cdot 10^5$
Natural interfaces		
c_0	(MPa)	0.0
f_t	(MPa)	0.0
G_{ft}	(Pa m)	0.0
G_{fs}	(Pa m)	0.0
ϕ	(°)	10
k_n, k_s	(MPa/m)	$1 \cdot 10^5$
Initial normal opening	(m)	$2.68 \cdot 10^{-8}$

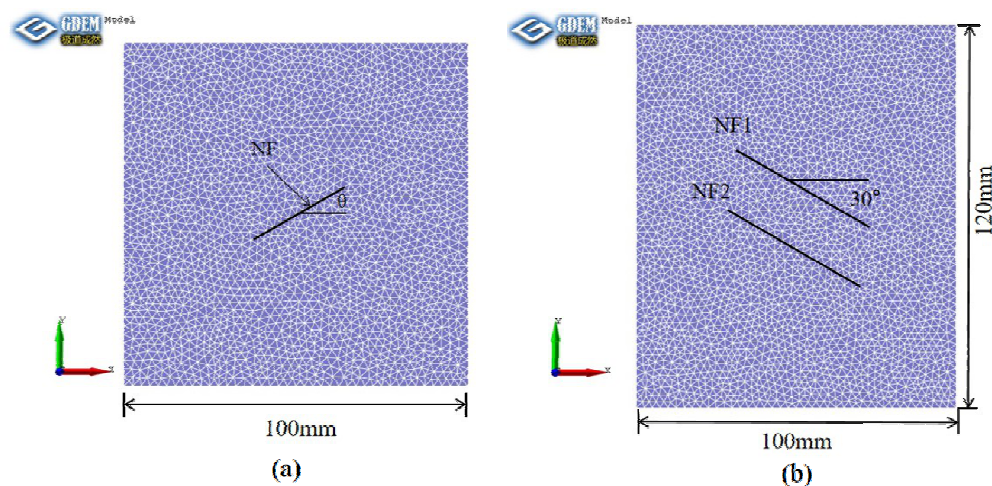


Fig. 2. Numerical models and meshes (a) square block, (b) rectangular block

The Mohr-Coulomb model is considered for shear failure of interfaces as

$$\begin{aligned}
 &\text{If } F_s(t_i) \geq F_n(t_i) \tan(\phi) + c_t(t_{i-1}) A_c \\
 &\text{Then } F_s(t_i) = F_n(t_i) \tan(\phi) + c_t(t_{i-1}) A_c \\
 &\text{with } c_n(t_{i-1}) = \max \left[c_0 - c_0^2 \frac{\Delta u_s(t_{i-1})}{2G_{fs}}, 0 \right]
 \end{aligned} \quad (5)$$

where c_0 is the initial cohesion, $c(t_{i-1})$ is the residual cohesion at the previous time step, ϕ is the internal friction angle and G_{fs} is the shear fracture energy.

Equations 4 and 5 indicate a linear softening relationship between cracking opening and traction, and other types of traction-separation laws, such as exponential, bilinear, and hyperbolic laws, can also be implemented [40–42] similarly.

2.3 Hydro-mechanical coupling

For the CDEM, the natural and new cracks are modelled directly with interfaces, and block elements and interface elements share the same node. Hence, based on the effect stress theory, the equivalent flow pressures s_p (s_f is the liquid saturation degree, and p is the pressure of the flow) can be directly applied on the cracks to account for the influence of flow pressure on cracks. Once cracks open, the seepage field is captured by the finite volume method (FVM), which has been discussed and applied in [43, 44]. The seepage velocity v of the fracturing fluid is

$$v = -\frac{k_{re} \lambda}{\mu} \frac{\partial p}{\partial x} \quad (6)$$

where k_{re} is the relative permeability coefficient, $k_{re} = s_f^2(3 - 2s_f)$; λ is the equivalent intrinsic permeability coefficient of cracks, and $\lambda = (\Delta du)^2 / 12$ is assumed; and μ is the viscosity of the flow.



3. Model Parameters

To examine the performance of fracture propagation and their interaction, a square block with one natural fracture and two natural fractures is simulated. The dimension of the first model is $0.1 \text{ m} \times 0.1 \text{ m}$, the model is divided by triangular mesh, which contains 4174 block elements and 2168 nodes. The size of the second model is $0.1 \text{ m} \times 0.12 \text{ m}$, which consists of 5026 block units and 2602 nodes; see Figure 2. The injection point is located in the middle of the model with a diameter of 0.006 m.

The material parameters are shown in Table 1. The initial geostress of the coal seam in the X direction is -10 MPa, and that in the Y direction is -5 MPa. The spring coefficients of the virtual interfaces are set to be consistent with the coal mass.

A detailed discussion of random strengths is provided in the next section. The calculation includes two stages: i) geostress balance: the geostress is applied to the model, ii) hydraulic fracturing: the time step is set to $1 \cdot 10^{-5} \text{ s}$, with a total calculation time of 6 s.

4. Results and Analysis

4.1 Influence of the natural fracture angle on the hydraulic fracture propagation

In this section, the influence of the natural fracture angle θ on hydraulic fracturing is analyzed. The fluid is injected into the block with constant flow rate $5 \times 10^{-7} \text{ m}^3/\text{s}$. The injection point is located at the center of the block.

As shown in Figure 3, the cracks mainly extend from the tips of the natural crack. When the geostress along the Y direction is larger than the value along the X direction, many vertical cracks appear. For the cases with $\theta = 0^\circ$ and $\theta = 90^\circ$, many small cracks appear that provide rich fracture networks.

The pressure at the injection point is shown in Figure 4(a), and the pressure has an obvious drop point because of crack propagation. When defining the maximum pressure before a sudden drop as the fracture pressure, the values considering different α are as shown in Figure 4(b). When the geostress along the X-axis is a high compression stress, the fracture pressure of $\theta = 90^\circ$ is the largest.

The fracture aperture curves under different angles are shown in Figure 5 (a). When the angles are 15° , 30° , 45° , 60° , 75° and 90° , the fracture apertures at the injection point are approximately $4.72 \times 10^{-6} \text{ m}$, $2.43 \times 10^{-6} \text{ m}$, $3.83 \times 10^{-6} \text{ m}$, $2.52 \times 10^{-6} \text{ m}$, $3.70 \times 10^{-6} \text{ m}$ and $5.23 \times 10^{-6} \text{ m}$, respectively. When θ between the natural fracture and X-direction is 45° and symmetrical, the size of the fracture opening also tends to be symmetrical and separate. For example, the difference between 30° and 60° is the smallest, the fracture opening curve is a "W" shape, and the fracture aperture at the injection point is the maximum when $\theta = 90^\circ$.

Figure 5(b) Shows the change curve of the rupture rate under different angles. The rupture rate curve presents an anti-symmetric distribution trend with an angle of 45° .

4.2 Influence of random strength on the hydraulic fracture propagation

The numerical analysis in this section adopts the random strength model to study and analyze the influence of the combination of randomly set geostress strengths on hydraulic fracture propagation. In the actual calculation, θ between the natural fracture and X-direction is set to 60° ; the density, Young's elastic modulus, and Poisson's ratio are kept consistent; and only the strength parameters are randomized. The random mode uses a uniform distribution mode, and when random, the mean value of each intensity parameter is guaranteed to be consistent with the above parameters. The random range of cohesion is 1-5 MPa, the random range of tensile strength is 1-5 MPa, and the random range of internal friction angle is $22\text{--}45^\circ$ (the expectation of the tangent value is consistent).

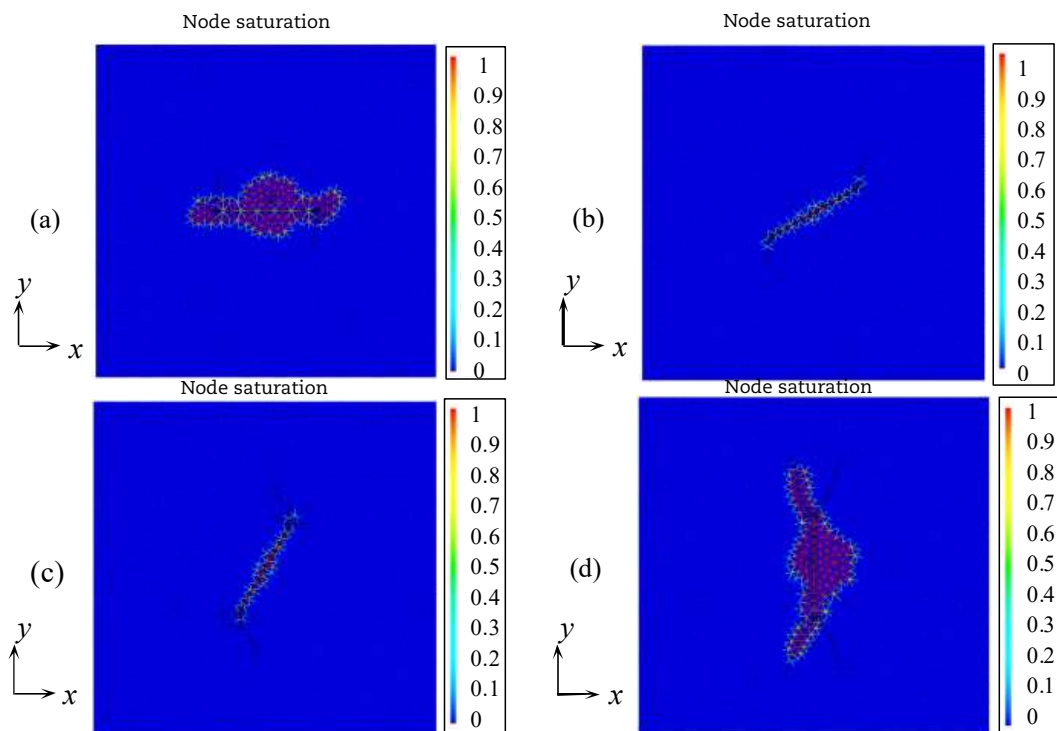


Fig. 3. Fracture propagation considering different angles: (a) $\theta = 0^\circ$, (b) $\theta = 30^\circ$, (c) $\theta = 60^\circ$, (d) $\theta = 90^\circ$



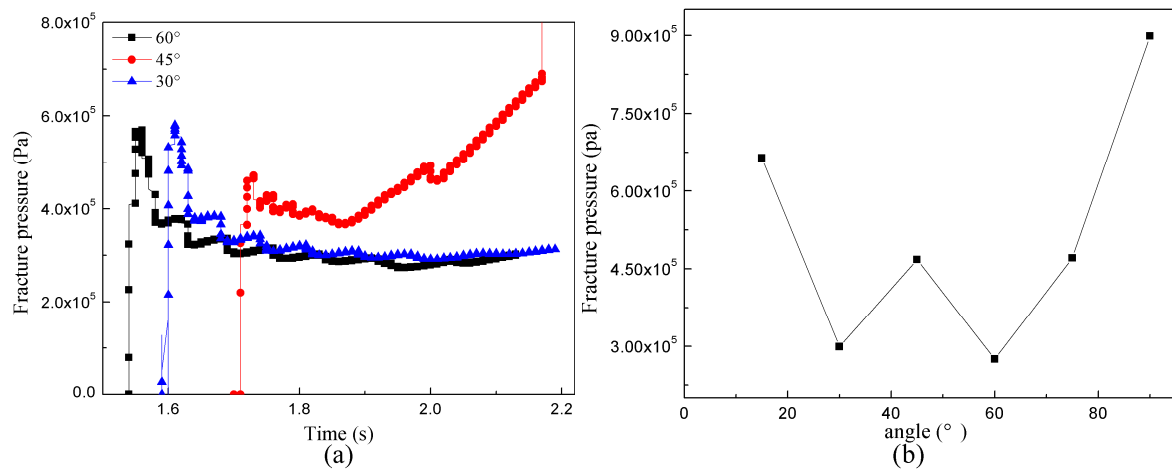


Fig. 4. (a) Pressures at the injection point, (b) Fracture pressures

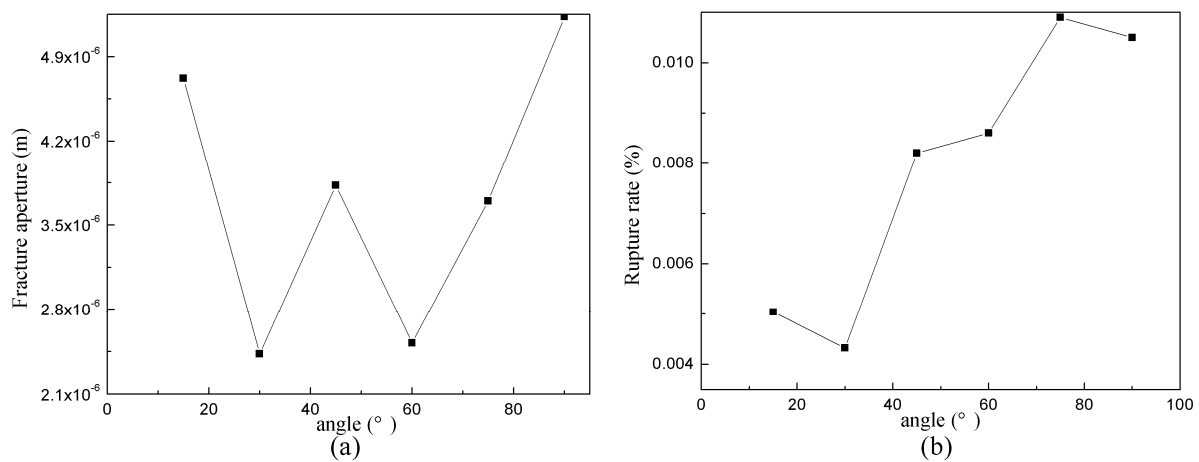


Fig. 5. Curve of fracture aperture and rupture rate, and (a) Fracture aperture change curve at different angles, (b) Rupture rate curve

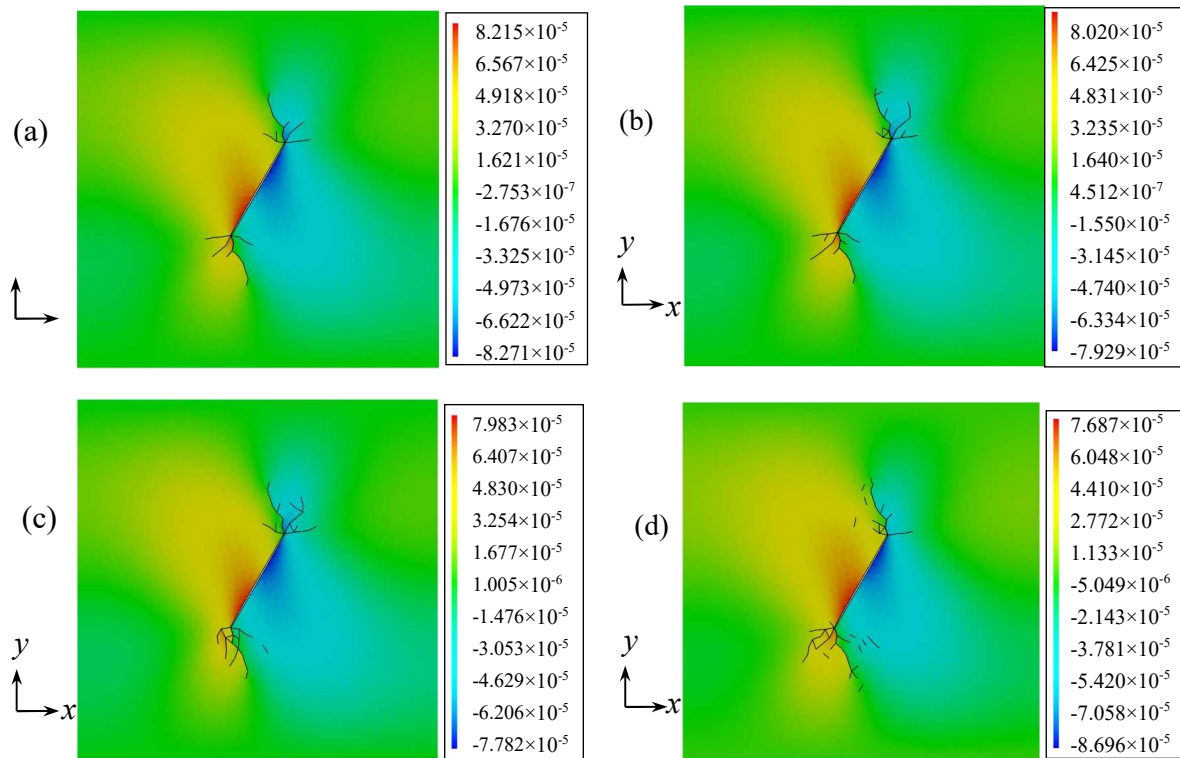


Fig. 6. Displacement diagram (units: mm), and (a) no, (b) C1, (c) C4, (d) C7



Table 2. Random strength combination table

Combination1 (C1)	cohesion
Combination2 (C2)	tension
Combination3 (C3)	friction
Combination4 (C4)	cohesion, tension
Combination5 (C5)	cohesion, friction
Combination6 (C6)	tension, friction
Combination7 (C7)	cohesion, tension, friction

The random influence of strength is analyzed through the combination of different strengths, and the combination is shown in Table 2. The fracture propagation results of the model are shown in Figure 6.

Figure 6 shows the displacement variation diagram under different combinations. The development of coal seam cracks without a random intensity setting involves slowly growing individual cracks. The development of coal seam cracks with random intensity settings is relatively rich, and there are many tiny cracks.

As shown in Figure 7(a), the fracture aperture changes under different combinations. The change trend of fracture aperture is the same, which is a gradual growth trend, and the growth rate becomes slower in the middle and later stages. As shown in Figure 7(b), the fracture pressure variation diagram under different combinations shows that the variation trend of fracture pressure is the same. Because the tensile strength of natural fractures is lower than that of coal seams, when natural fractures start to crack, the fracture pressure at the injection point suddenly decreases and then gradually decreases to a flat level.

As shown in Figure 8, the variation diagram of coal seam fracture degree under different combinations shows that combination 5 has the highest fracture rupture rate, and the combination with friction has a higher value, which also shows that the fracture rupture rate is more sensitive to friction, followed by cohesion and finally tension.

4.2 Influence of permeability change on the hydraulic fracture propagation

In this section, the influence of a coal seam permeability change on hydraulic fracture propagation is studied and analyzed. Here, θ between the natural fracture and X direction of the coal seam is set as 60° , and the random mode of geostress intensity is a uniform distribution mode. Combination 7 (C7) in Table 2 is adopted.

Figure 9 shows the diagram of coal seam fracture saturation under different permeabilities. When the permeability is very low, the fluid tends to persist in the fracture and does not diffuse out. If the permeability increases, the fluid gradually seeps out, and the fracture also expands outward.

Figure 10 shows the fracture aperture and fluid volume transformation curves under different permeabilities. With the gradual increase in permeability, the values of the two fluctuate slightly, but the overall trend declines.

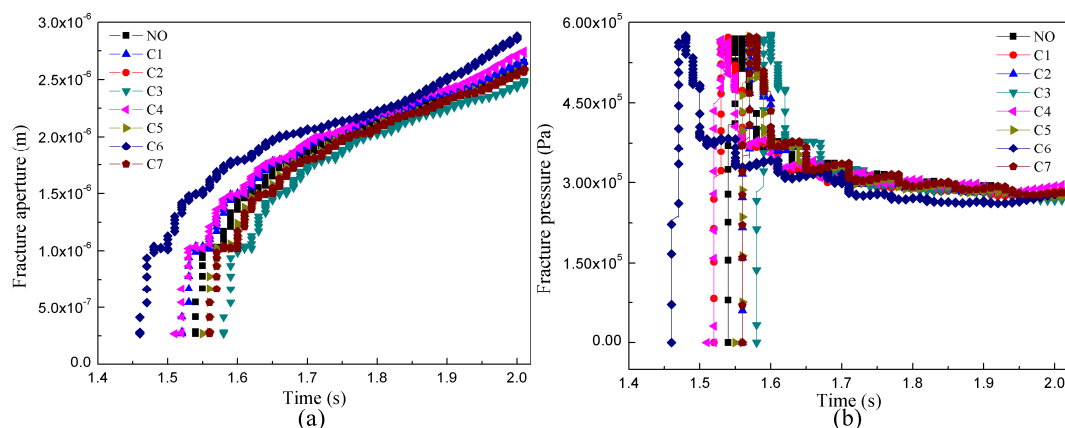


Fig. 7. Variation curve of fracture aperture and fracture pressure, and (a) Fracture aperture diagram at random intensity, (b) Fracture pressure diagram at random intensity

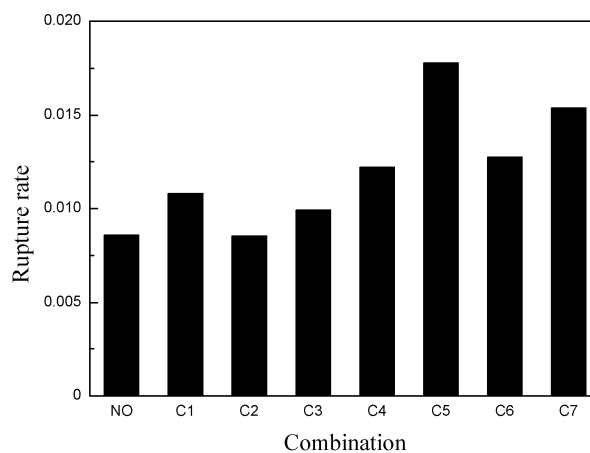


Fig. 8. Fracture rupture rate curve



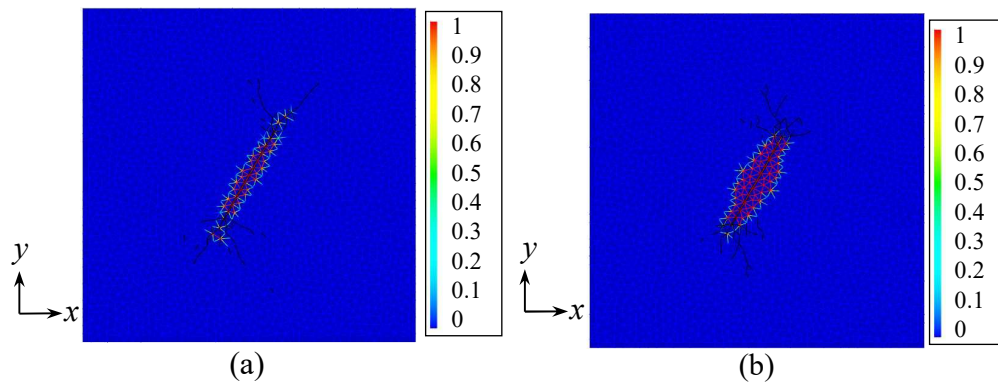


Fig. 9. Diagram of seam fracture saturation, and (a) permeability is $0.06 \times 10^{-14} \text{ m}^2$, (b) permeability is $0.5 \times 10^{-14} \text{ m}^2$

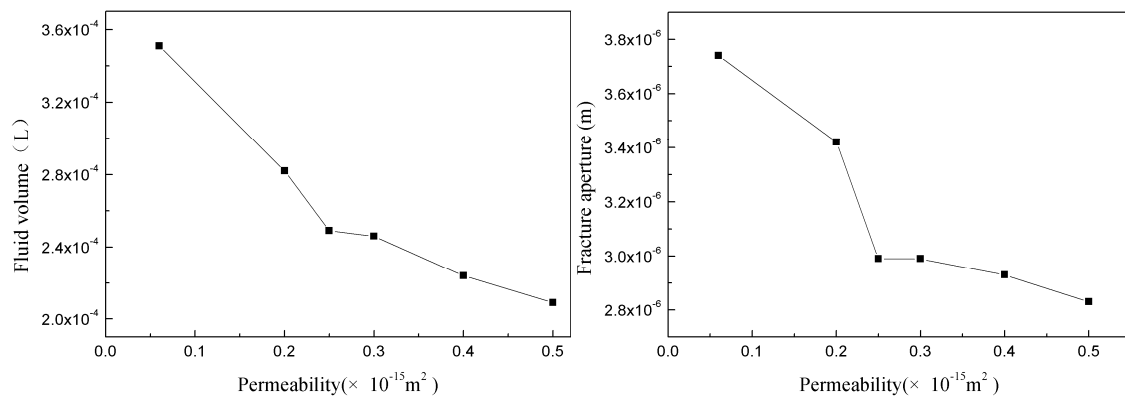


Fig. 10. The relationship between fracture aperture, fluid volume and permeability coefficient

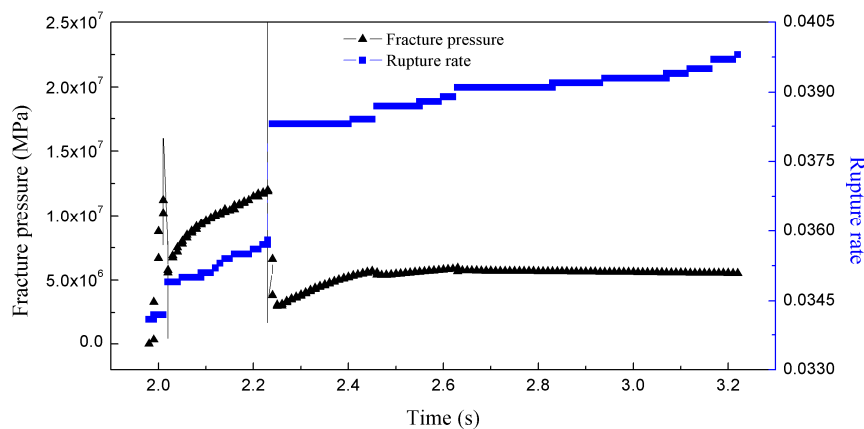


Fig. 11. The fracture pressure and rupture rate as function of time

4.3 Influence of horizontal geostress difference on hydraulic fracture propagation

In this section, the influence rule of the horizontal geostress difference of the coal seam on hydraulic fracture propagation is analyzed. Two natural fractures are set 10 mm away from the injection port. The natural fracture is 50 mm long and $1 \times 10^{-6} \text{ m}$ wide, with an angle of 30° to the X direction. The geostress differences are set as 0 MPa, 3 MPa, 179.5 MPa, 7 MPa, 10 MPa and 12 MPa.

Figure 11 shows the curve of fracture pressure and rupture rate over time at the entrance of hydraulic fracturing. Here, 2.0 s is the time of fracture initiation, and at approximately 2.0 s, the hydraulic fracture begins to crack from the injection port and continues to expand. Over 2.0 s-2.2 s, the hydraulic fracture meets the natural fracture, the fracture pressure at the injection port suddenly drops, the fracture degree increases suddenly, the hydraulic fracture expands along the natural fracture direction, and the direction changes. After 2.2 s, the hydraulic fracture expands in the natural fracture. The fracture pressure at the injection port increases slowly and then remains stable, and the rupture rate increases gradually.

The process of hydraulic fracture propagation under different geostress differences is shown in Figure 12. The numerical results show that under the action of two natural fractures, the hydraulic fracture can expand through three paths: (1) When the horizontal geostress difference is 12 MPa and 10 MPa, the hydraulic fracture first propagates along the direction perpendicular to the minimum principal stress. After intersecting with the natural fracture, the hydraulic fracture activates the natural fracture and preferentially propagates from the right end of the second natural fracture (as shown in Figure 12(e), (f)). (2) When the horizontal geostress difference is 7 MPa and 5 MPa, the hydraulic fracture preferentially propagates along the left end of the first natural fracture (as shown in Figure 12(c), (d)). (3) When the horizontal geostress difference is 3 MPa and 0 MPa, the hydraulic fracture propagates along the left direction of the first natural fracture and the right direction of the second natural fracture (as shown in Figure 12(a), (b)). In the first two paths, the scope of hydraulic fracture propagation is narrow, and the number of fractures is small; in the third path, the number of fractures is large, and the expansion range is wide.



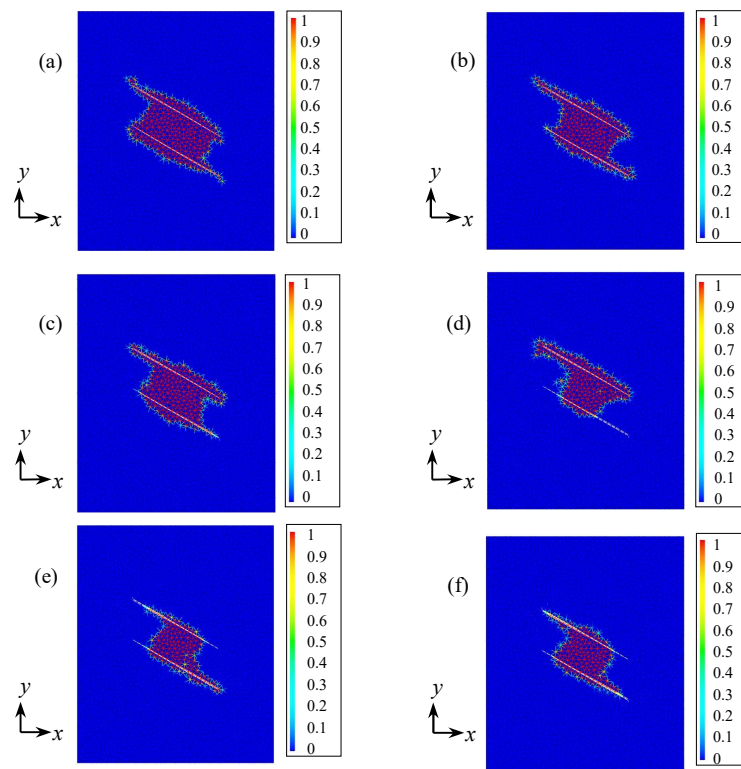


Fig. 12. Propagation processes of a hydraulic fracture under the action of a natural fracture, and the horizontal geostress difference is (a) 0 MPa, (b) 3 MPa, (c) 5 MPa, (d) 7 MPa, (e) 10 MPa, (f) 12 MPa

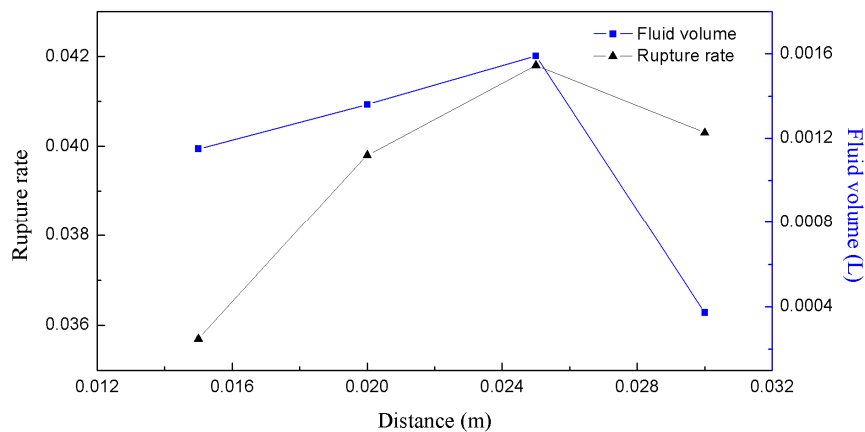


Fig. 13. Rupture rate and fluid volume as function of distance

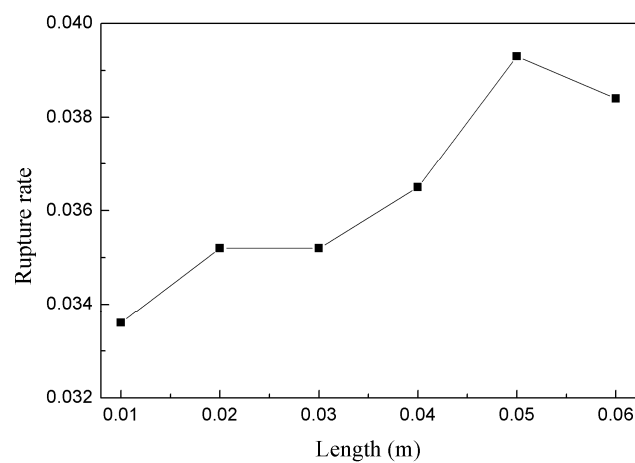


Fig. 14. Rupture rate as function of length



The extension direction of hydraulic fractures depends on the difference in geostress. The hydraulic fracture is parallel to the maximum horizontal principal stress, but the hydraulic fracture does not always extend along a specific direction. In the process of extension, the natural fracture extends along the natural fracture direction, that is, the hydraulic fracture changes in direction, forming a more abundant fracture network. The larger the geostress difference is, the less likely the natural fracture opens. The smaller the geostress difference is, the more hydraulic fractures tend to penetrate into natural fractures. A low geostress difference is conducive to the opening of natural fractures and the uniform development of fracture networks.

4.4 Influence of fracture distance and length variation on hydraulic fracture propagation

We keep the natural fractures above the injection port in place and adjust the positions of the natural fractures below the injection port so that the spacing is 0.015 m, 0.020 m, 0.025 m, and 0.03 m to study the effect of changes in natural fracture distance on hydraulic fractures.

The relationship between fracture volume and fracture rate is shown in Figure 13. Specifically, with increasing fracture distance, the rupture rate and fluid volume in the fracture increase. When the distance between two fractures is 0.025 m, the rupture rate and fluid volume are the largest, and the range of the fracture network is the largest. When the fracture distance is greater than 0.025 m, the fracture rate and fluid volume decrease. This is because the hydraulic fractures do not fully communicate with the natural fractures in time, resulting in a decrease in the fracture propagation area. The optimal fracture distance is 0.025 m. Because the hydraulic fracture and natural fracture communicate well, the fracture network expands sufficiently, and the fracture rate and fluid volume in the fracture reach the peak.

Keep the natural fracture above the injection port still and adjust the length of the natural fracture below the injection port to 0.01 m, 0.02 m, 0.03 m, 0.04 m, 0.05 m and 0.06 m. The influence of natural fracture length on hydraulic fracture propagation is studied.

Figure 14 shows the relationship between fracture length and rupture rate. With increasing fracture length, the fracture range near the natural fracture increases, and the rupture rate increases. When the fracture length is 0.05 m, that is, when the lengths of the two fractures are equal, the fracture rate is the largest. As the fracture continues to grow, the rupture rate of the coal seam decreases, which also indicates that the longer the natural fracture is, the greater the hydraulic fracture along the natural fracture. Therefore, when the lengths of the two natural fractures are equal, the rupture rate is the largest, and the hydraulic fracture network range is the largest.

5. Conclusion

In this paper, the Mohr-Coulomb model of brittle fracture and the coupling model of fracture seepage and stress are introduced into the continuous-discontinuous element method to simulate the hydraulic fracturing of coal seams with natural fractures. The conclusions are as follows:

- Effect of angle θ : The larger the angle θ between the natural fracture and X-direction is, the smaller the fractures and the more abundant the fracture network. The fracture pressure and fracture aperture at the injection point are symmetrically distributed at an angle of 45° , and the fracture degree curve is antisymmetric.
- Effect of random strength: The development of hydraulic fractures in coal seams with random strength is more abundant, there are many micro-fractures, and the fracture degree is the most sensitive to friction.
- Effect of permeability: With increasing permeability, the fracture degree, fluid volume and fracture opening of the coal seam show a downward trend.
- Effect of horizontal geostress difference: The larger the horizontal geostress difference is, the less likely the natural fracture is to open. The smaller the geostress difference is, the more hydraulic fractures tend to penetrate into natural fractures. A low geostress difference is conducive to the opening of natural fractures and the uniform development of fracture networks.
- Effect of natural fracture distance and length: With increasing fracture distance and length, the fracture rate of the coal seam increases. A distance of 0.025 m and a length of 0.05 m are the optimal distance and length; in other words, when two natural fractures are symmetrically and equally distributed on both sides of the injection point, the hydraulic fracture and natural fracture communicate well, the fracture network expands fully, the fracture rate reaches the peak, and the hydraulic fracture network has the largest range.

Hydraulic fractures are parallel to the maximum horizontal principal stress, but natural fractures can change the development path of hydraulic fractures. When natural fractures exist, hydraulic fractures develop along the direction of natural fractures, forming a more abundant fracture network. The angle θ between the natural fracture and the X-direction, horizontal geostress difference and natural fracture distance has a predominant effect on the opening degree of the natural fracture.

Author Contributions

“Conceptualization, Zizheng Sun, Chun Feng; Methodology, Chun Feng; Software, Chun Feng; Validation, Hui Gao, Zizheng Sun; Formal Analysis, Hui Gao, Zizheng Sun; Investigation, Haifeng Zhou, Zizheng Sun; Data Curation, Haifeng Zhou, Hui Gao; Writing-Original Draft Preparation, Haifeng Zhou, Hui Gao, Zizheng Sun; Writing—Review & Editing, Zizheng Sun; Visualization, Hui Gao, Haifeng Zhou; Supervision, Zizheng Sun; Project Administration, Zizheng Sun; Funding Acquisition, Haifeng Zhou, Zizheng Sun. The manuscript was written through the contribution of all authors. All authors discussed the results, reviewed, and approved the final version of the manuscript

Conflict of Interest

The authors declared no potential conflicts of interest concerning the research, authorship, and publication of this article.

Funding

The authors wish to acknowledge the financial support from the China Postdoctoral Science Foundation (No. 2020T130377), Shandong Postdoctoral Innovation Project Foundation (No. 202001012) and Shenzhen Collaborative Innovation and Technology Plan Foundation.



Data Availability Statements

The datasets generated and/or analyzed during the current study are available from the corresponding author on reasonable request.

Nomenclature

v_i, u_i	The generalized coordinates	$\Delta u_s(t_i)$	The shear relative displacement (crack opening) at the present time step
L	The energy of the Lagrangian system	$\sigma_i(t_{i-1})$	The residual tensile strength at the last time step
Q_i	The work of non-conservative forces	G_{ft}	The tensile fracture energy
$\Delta \varepsilon_{ij}$	The increment strain tensor	c_0	The initial cohesion
$\Delta \theta$	The volumetric strain	$c(t_{i-1})$	The residual cohesion at the previous time step
K	The bulk	ϕ	The internal friction angle
G	Shear modulus	G_{fs}	The shear fracture energy
$\Delta \sigma_{ij}$	The incremental stress tensor	s_f	The liquid saturation degree
δ_{ij}	The Kronecker mark	p	The pressure of the flow
t_i	The last time steps	k_{re}	The relative permeability coefficient
t_{i-1}	Present time steps	λ	The equivalent intrinsic permeability coefficient of cracks
$\Delta u_n(t_i)$	The normal relative displacement (crack opening) at the present time step	μ	The viscosity of the flow

Abbreviations

The following abbreviations are used in this manuscript:

CDEM	Continuum-discontinuum Element Method
FEM	Finite Element Method
XFEM	eXtended Finite Element Method
CPM	Cracking Particle Method
CEM	Cracking Elements Method
FVM	Finite Volume Method

References

- [1] Areias, P., Reinoso, J., Camanho, P., Rabczuk, T., A constitutive-based element-by-element crack propagation algorithm with local mesh refinement, *Computational Mechanics*, 56(2), 2015, 291–315.
- [2] Areias, P., Rabczuk, T., Dias-da-Costa, D., Element-wise fracture algorithm based on rotation of edges, *Engineering Fracture Mechanics*, 110, 2013, 113–137.
- [3] Areias, P., Rabczuk, T., Finite strain fracture of plates and shells with configurational forces and edge rotations, *International Journal for Numerical Methods in Engineering*, 94(12), 2013, 1099–1122.
- [4] Areias, P., Rabczuk, T., Steiner-point free edge cutting of tetrahedral meshes with applications in fracture, *Finite Elements in Analysis and Design*, 132, 2017, 27–41.
- [5] Areias, P., Rabczuk, T., César de Sá, J., A novel two-stage discrete crack method based on the screened Poisson equation and local mesh refinement, *Computational Mechanics*, 58(6), 2016, 1003–1018.
- [6] Ooi, E., Shi, M., Song, C., Tin-Loi, F., Yang, Z. Dynamic crack propagation simulation with scaled boundary polygon elements and automatic remeshing technique, *Engineering Fracture Mechanics*, 106, 2013, 1–21.
- [7] Miehe, C., Hofacker, M., Schänzel, L.M., Aldakheel, F., Phase field modeling of fracture in multi-physics problems. Part II. Coupled brittle-to-ductile failure criteria and crack propagation in thermo-elastic-plastic solids, *Computer Methods in Applied Mechanics and Engineering*, 294, 2015, 486–522.
- [8] Wu, J.Y., Nguyen, V.P., A length scale insensitive phase-field damage model for brittle fracture, *Journal of the Mechanics and Physics of Solids*, 119, 2018, 20–42.
- [9] Wu, J.Y., Robust numerical implementation of non-standard phase-field damage models for failure in solids, *Computer Methods in Applied Mechanics and Engineering*, 340, 2018, 767–797.
- [10] Zhou, S.W., Rabczuk, T., Zhuang, X.Y., Phase field modeling of quasi-static and dynamic crack propagation: COMSOL implementation and case studies, *Advances in Engineering Software*, 122, 2018, 31–49.
- [11] Hofacker, M., Miehe, C., A phase field model of dynamic fracture: Robust field updates for the analysis of complex crack patterns, *International Journal for Numerical Methods in Engineering*, 93(3), 2013, 276–301.
- [12] Cervera, M., Chiumenti, M., Codina, R., Mixed stabilized finite element methods in nonlinear solid mechanics: Part I: Formulation, *Computer Methods in Applied Mechanics and Engineering*, 199(37), 2010, 2559–2570.
- [13] Cervera, M., Chiumenti, M., Codina, R., Mixed stabilized finite element methods in nonlinear solid mechanics: Part II: Strain localization, *Computer Methods in Applied Mechanics and Engineering*, 199(37), 2010, 2571–2589.
- [14] Cervera, M., Chiumenti, M., Benedetti, L., Codina, R., Mixed stabilized finite element methods in nonlinear solid mechanics. Part III: Compressible and incompressible plasticity, *Computer Methods in Applied Mechanics and Engineering*, 285, 2015, 752–775.
- [15] Cervera, M., Chiumenti, M., Codina, R., Mesh objective modeling of cracks using continuous linear strain and displacement interpolations, *International Journal for Numerical Methods in Engineering*, 87(10), 2011, 962–987.
- [16] Lafontaine, N.M., Rossi, R., Cervera, M., Chiumenti, M., Explicit mixed strain-displacement finite element for dynamic geometrically non-linear solid mechanics, *Computational Mechanics*, 55(3), 2015, 543–559.
- [17] Cervera, M., Chiumenti, M., Smeared crack approach: back to the original track, *International Journal for Numerical and Analytical Methods in Geomechanics*, 30(12), 2006, 1173–1199.
- [18] Chiumenti, M., Cervera, M., Moreira, C.A., Barbat, G.B., Stress, strain and dissipation accurate 3-field formulation for inelastic isochoric deformation, *Finite Elements in Analysis and Design*, 192, 2021, 103534.
- [19] Wu, J.Y., Li, F.B., An improved stable XFEM (Is-XFEM) with a novel enrichment function for the computational modeling of cohesive cracks, *Computer Methods in Applied Mechanics and Engineering*, 295, 2015, 77–107.
- [20] Song, J.H., Areias, P., Belytschko, T., A method for dynamic crack and shear band propagation with phantom nodes, *International Journal for Numerical Methods in Engineering*, 67, 2006, 868–893.
- [21] Bybordiari, M., da Costa, D.D., A consistent finite element approach for dynamic crack propagation with explicit time integration, *Computer Methods in Applied Mechanics and Engineering*, 376, 2021, 113652.
- [22] Zheng, H., Xu, D., New strategies for some issues of numerical manifold method in simulation of crack propagation, *International Journal for*



Numerical Methods in Engineering, 97(13), 2014, 986–1010.

[23] Zheng, H.Z., Liu, F., Du, X.L., Complementarity problem arising from static growth of multiple cracks and MLS-based numerical manifold method, *Computer Methods in Applied Mechanics and Engineering*, 295, 2015, 150–171.

[24] Wu, Z.J., Ngai, L., Wong, Y., Frictional crack initiation and propagation analysis using the numerical manifold method, *Computers and Geotechnics*, 39, 2011, 38–53.

[25] Wu, Z.J., Fan, L.F., Liu, Q.S., Ma, G.W., Micro-mechanical modeling of the macro-mechanical response and fracture behavior of rock using the numerical manifold method, *Engineering Geology*, 225, 2017, 49–60.

[26] Dias, I.F., Oliver, J., Lemos, J.V., Lloberas-Valls, O., Modeling tensile crack propagation in concrete gravity dams via crack-path-field and strain injection techniques, *Engineering Fracture Mechanics*, 154, 2016, 288–310.

[27] Dias-da-Costa, D., Alfaiate, J., Sluys, L.J., Areias, P., Júlio, E., An embedded formulation with conforming finite elements to capture strong discontinuities, *International Journal for Numerical Methods in Engineering*, 93(2), 2012, 224–244.

[28] Dias-da-Costa, D., Cervenka, V., Graça-e-Costa, R., Model uncertainty in discrete and smeared crack prediction in RC beams under flexural loads, *Engineering Fracture Mechanics*, 199, 2018, 532–543.

[29] Zhang, Y., Zhuang, X., Cracking elements: a self-propagating Strong Discontinuity embedded Approach for quasi-brittle fracture, *Finite Elements in Analysis and Design*, 144, 2018, 84–100.

[30] Zhang, Y., Zhuang, X., Cracking elements method for dynamic brittle fracture, *Theoretical and Applied Fracture Mechanics*, 102, 2019, 1–9.

[31] Zhang, Y., Mang, H.A., Global cracking elements: a novel tool for Galerkin-based approaches simulating quasi-brittle fracture, *International Journal for Numerical Methods in Engineering*, 121, 2020, 2462–2480.

[32] Mu, L., Zhang, Y., Cracking elements method with 6-node triangular element, *Finite Elements in Analysis and Design*, 177, 2020, 103421.

[33] Rabczuk, T., Belytschko, T., Adaptivity for structured meshfree particle methods in 2D and 3D, *International Journal for Numerical Methods in Engineering*, 63(11), 2005, 1559–1582.

[34] Zhuang, X., Augarde, C.E., Mathisen, K.M., Fracture modeling using meshless methods and level sets in 3D: framework and modeling, *International Journal for Numerical Methods in Engineering*, 92(11), 2012, 969–998.

[35] Zhuang, X., Augarde, C., Bordas, S., Accurate fracture modelling using meshless methods, the visibility criterion and level sets: Formulation and 2D modelling, *International Journal for Numerical Methods in Engineering*, 86, 2011, 249–268.

[36] Rabczuk, T., Bordas, S., Zi, G., On three-dimensional modelling of crack growth using partition of unity methods, *Computers and Structures*, 88(23), 2010, 1391–1411.

[37] Rabczuk, T., Belytschko, T., Cracking particles: a simplified meshfree method for arbitrary evolving cracks, *International Journal for Numerical Methods in Engineering*, 61, 2004, 2316–2343.

[38] Rabczuk, T., Belytschko, T., A three-dimensional large deformation meshfree method for arbitrary evolving cracks, *Computer Methods in Applied Mechanics and Engineering*, 196(29), 2006, 2777–2799.

[39] Rabczuk, T., Zi, G., Bordas, S., Nguyen-Xuan, H., A simple and robust three-dimensional cracking-particle method without enrichment, *Computer Methods in Applied Mechanics and Engineering*, 199(37), 2010, 2437–2455.

[40] Meschke, G., Dumstorff, P., Energy-based modeling of cohesive and cohesiveness cracks via X-FEM, *Computer Methods in Applied Mechanics and Engineering*, 196(21), 2007, 2338–2357.


[41] Mosler, J., Meschke, G., 3D modelling of strong discontinuities in elastoplastic solids: fixed and rotating localization formulations, *International Journal for Numerical Methods in Engineering*, 57(11), 2003, 1553–1576.

[42] Zhang, Y., Zhuang, X., A softening-healing law for self-healing quasi-brittle materials: analyzing with strong discontinuity embedded approach, *Engineering Fracture Mechanics*, 192, 2018, 290–306.


[43] Sun, Z., Yan, X., Liu, R., Xu, Z., Li, S., Zhang, Y., Transient Analysis of Grout Penetration With Time-Dependent Viscosity Inside 3D Fractured Rock Mass by Unified Pipe-Network Method, *Water*, 10(9), 2018, 1122.


[44] Sun, Z., Yan, X., Han, W., Ma, G., Zhang, Y., Simulating the Filtration Effects of Cement-Grout in Fractured Porous Media with the 3D Unified Pipe-Network Method, *Processes*, 7(1), 2019, 46.

ORCID iD

Haifeng Zhou  <https://orcid.org/0000-0002-8988-5727>

Hui Gao  <https://orcid.org/0000-0002-1964-2914>

Chun Feng  <https://orcid.org/0000-0001-6592-144X>

Zizheng Sun  <https://orcid.org/0000-0002-3874-6575>



© 2021 Shahid Chamran University of Ahvaz, Ahvaz, Iran. This article is an open access article distributed under the terms and conditions of the Creative Commons Attribution-NonCommercial 4.0 International (CC BY-NC 4.0 license) (<http://creativecommons.org/licenses/by-nc/4.0/>).

How to cite this article: Zhou H., Gao H., Feng C., Sun Z. Simulation of Hydraulic Fracture Propagation in Fractured Coal Seams with Continuum-discontinuum Elements, *J. Appl. Comput. Mech.*, 7(4), 2021, 2185–2195.
<https://doi.org/10.22055/JACM.2021.37475.3022>

Publisher's Note Shahid Chamran University of Ahvaz remains neutral with regard to jurisdictional claims in published maps and institutional affiliations.

